# Transition and gas leakage mechanisms of ventilated cavities around a conical axisymmetric body

Liang Hao,[1] Decai Kong,[1,2] Yue Wu,[1,*] Taotao Liu,[1,3] and Guoyu Wang[1,3]
[1]*School of Mechanical Engineering, Beijing Institute of Technology, Beijing 100081, China*
[2]*China Academy of Launch Vehicle Technology, Beijing 100076, China*
[3]*Beijing Institute of Technology Chongqing Innovation Center, Chongqing 401120, China*

(Received 15 May 2022; accepted 4 November 2022; published 5 December 2022)

In this paper, we present an experimental investigation on gas entrainment and gas leakage mechanisms of different ventilated cavity flow patterns around a conical axisymmetric body, by high-speed video and theoretical analysis. The ventilated cavity is generated around a conical axisymmetric body and studied in the closed-loop water tunnel at Lab of Fluid Machinery and Engineering, Beijing Institute of Technology. The experimental studies revealed three distinct cavity patterns, namely, the foamy cavity (FC), the intermittent and transitional cavity (ITC), and the continuous and transparent cavity (CTC) under different Froude and $C_Q$ values. All patterns contain the transparent region at the cavity rear (except FC) and the recirculating vortex that generates foam shedding at the cavity rear. The qualitative gas entrainment and leakage process are then explained based on the schematics of internal gas flow and surrounding water flow. As the flow pattern varies from FC to CTC with increasing ventilation rate, it is observed that the size of shedding foam grows larger while the shedding frequency gradually reduces, leading to balanced gas injection and leakage. Moreover, the mechanism controlling the hysteresis of the ITC-to-CTC transition is quantitatively explained using a gas leakage model of ITC cavities, which assumes the foam is periodically shed in the form of a vortex ring. After extensive validation by both current measurements and previous research, the model can accurately predict the ventilation rate required for the ITC-to-CTC transition. Finally, the mechanism causing closure discrepancy between CTC cavities in this paper and free-standing supercavities (without cavitator body) in past studies are investigated. Due to the impact of stagnation points on the cavitator body, the adverse pressure gradient (APG) in the streamwise direction of CTC cavities is estimated to be 6.8 times that of free-standing supercavities under the same flow conditions, leading to water flow separation at the cavity rear. As a result, after the ventilation hysteresis, the recirculating vortex closure is still observed in CTC cavities under the impact of large APG, different from free-standing supercavities that form vortex tube closure.

DOI: 10.1103/PhysRevFluids.7.123901

## I. INTRODUCTION

Ventilated cavitation is formed by artificially injecting noncondensable gas into the low-pressure region around an underwater vehicle to create a bubble of gas in water [1–5]. This technology is considered an effective method to increase the cavity pressure $P_c$ [6–11] to weaken the cavity collapse load. More importantly, it can reduce the skin friction drag on the object up to 90% to achieve high-speed underwater when the cavity is large enough to encompass the entire object

*wuyue@bit.edu.cn

 

[2,12–14], e.g., high-speed underwater vehicles for naval applications. Therefore, it is significant to analyze the ventilated cavitating flow, which has been investigated by many researchers through theorical, experimental, and numerical methods [15–18].

According to past papers, for ventilated cavitation reported by Reichardt [19], the conditions required to form and sustain a supercavity (a cavity covering the whole cavitator with a clear gas-water interface) are key questions. For decades, most studies on ventilated cavitating flow have been focused on elucidating the relations between different flow conditions and varied cavitator designs to establish stable supercavities. There has been much research on ventilated supercavities formed by different ventilation conditions, including several closure mechanisms, the relationships between the gas entrainment/leakage, and closure modes [5,18,20–23]. Some researchers derived the empirical or semi-empirical relations between the formations and transitions of closure modes, such as re-entrant jet (RJ), twin vortex (TV), quad vortex (QV), and pulsating cavity (PC). For instance, Campbell and Hilborne [24] conducted ventilated supercavitation experiments in a whirling arm channel for a limited range of Froude numbers (Fr) from 5 to 25, indicating a RJ cavity occurs at $\sigma_c \mathrm{Fr} > 1$ and a TV cavity forms at $\sigma_c \mathrm{Fr} < 1$. Spurk [25] experimentally investigated the ventilated supercavity shape and established a theoretical gas loss formulation for a high Fr on the assumption that the gas is entrained in the boundary layer formed at the liquid-gas interface to flow downstream. Kawakami and Arndt [26] and Karn *et al.* [27] further experimentally investigated the transition between the foamy cavity (FC) and the transparent ventilated supercavity. Then they observed two distinct types of RJs, which occurred in FC and during the transition between the RJ and TV closure modes of an unstable supercavity, respectively. In addition, they observed the QV closure mode after Kapankin and Gusev [28], which is a special case of stable vortex closure. Another group of research focused on the mechanism explanation of the gas entrainment and closure modes for ventilated supercavities. For example, Silberman and Song [29] found that, at high air entrainment rates, the entire supercavity has a wavy surface and the closure mode would transition to PC closure. The gas loss is primarily due to air pockets intermittently broken from the end of the cavity. Skidmore [22] further investigated the PC closure mechanism and pointed out that the liquid-gas interface pulsation was closely related to the Kelvin-Helmholtz instability. Recently, authors of several studies proposed some gas leakage and closure mechanisms of a ventilated supercavity. Karn *et al.* [5] observed hybrid closure modes in the experiments at Saint Anthony Falls Laboratory, such as hybrid QV and RJ closure (QVRJ) and hybrid TV and QV closure (TVQV). Additionally, they analyzed the gas leakage mechanism and further determined the conditions governing the occurrence of different closure modes. Wu *et al.* [23] and Lv *et al.* [30] further elucidated the transition mechanisms between the RJ and TV closure modes from the perspective of the flow structure inside ventilated supercavities. It was concluded in these works that the RJ mode is originated from the water flow separation at the cavity rear, and the TV mode is caused by the vortex shedding from three-dimensional (3D) asymmetric shape of the supercavity.

It is noteworthy that authors of most studies focused on free-standing ventilated supercavitation, which refers to the fact that the cavity does not enclose a solid object or interact with any solid surfaces downstream of the cavitator. Research focused on the cavity formation and development affected by interactions between the cavity and the solid surface does not receive much attention. Kawakami and Arndt [26], Lee *et al.* [31], and Shao *et al.* [32] used the mounting strut forward-facing model to generate supercavities where there is nonnegligible interaction between the cavity and the strut surface. This interaction has an impact on the transition between the FC and the transparent supercavity, namely, the ventilation demand for a stable supercavity. However, the struts used in their works are much thinner than the cavitator size, so that the contact area between cavity flow and strut surface is too small to cause critical changes on the gas entrainment and closure modes of the cavities. In these cases, conclusions for free-standing supercavities are also applicable. To further investigate the effect of interactions between the cavity and solid surface, in our previous studies [33,34], the ventilated cavities around a conical axisymmetric body with a conical headform and a column of the same size was studied. Here, we use *cavities* instead of *supercavity* since many interesting cavity patterns that do not enclose the body are observed

and discussed in our works. It is found that the cavity behaviors, such as cavity geometry, bubble dynamics, and closure modes, presented a significant variation during the transition from the FC to the transparent supercavity. Hence, different classifications of flow patterns are established other than that of free-standing supercavities, such as continuous transparent and asymmetric cavity (CTAC), bubbly cavity (BC), continuous transparent and BC (CTBC), continuous transparent and FC (CTFC), and hybrid continuous and FC (CFC). In recent years, other researchers also carried out some studies on ventilated cavitation flow around an axisymmetric body. For example, Sun *et al.* [35] also observed three unsteady flow patterns (FC, CTFC, and CTAC) at the development stage of ventilated cavitating flow. Moreover, they further investigated the shedding processes and vortex structures by combining numerical methods [36]. Wang *et al.* [37] and Lv *et al.* [30] analyzed the unsteady shedding behaviors of ventilated cavitating flow via experimental and numerical methods. They found that, due to the movement of the RJ, the cavity experiences three stages: rapid growth, growth with small pulsation, and periodic shedding. However, these studies did not substantially ascertain the physical mechanisms of formation and transition of different ventilated cavity flow patterns. In addition, the mechanisms of gas entrainment and gas leakage are not well understood for cavities with noticeable effects of interaction between the cavity flow and the solid surface.

Hence, to elucidate the physical mechanisms of ventilated cavitation around an axisymmetric body, in this paper, we further analyze the experimental results based on our previous studies [33,34] and explain the mechanisms of flow pattern formation/transition and gas entrainment/leakage. The structure of this paper is arranged as follows: Sec. II presents the experimental setup and method. Section III investigates the characteristics of ventilated cavitating flow around a conical axisymmetric body. Finally, the conclusions are drawn in Sec. IV.

## II. EXPERIMENTAL SETUP

The experimental studies are conducted in the Lab of Fluid Machinery and Engineering (LFME) closed-loop cavitation tunnel of Beijing Institute of Technology, which was introduced in previous studies in detail [33,34]. The rectangular test section is designed with nominal dimensions of $0.7 \times 0.19 \times 0.07$ m (length, height, and width) with three transparent walls for flow visualization. A corner vane and a straightening vane are equipped to reduce and weaken the flow turbulence level. In addition to that, a tank with a volume of $5\,\mathrm{m}^3$ is applied to separate the needless and undesirable bubbles in the flow. In the experiments, the main parameters, velocity and pressure, upstream are measured by an electromagnetic flowmeter with the maximum uncertainty of 0.5% and a vacuometer with the maximum uncertainty of 0.25%. The tunnel can generate the upstream with speeds up to 20 m/s.

The schematics of the experimental setup and the cavitator for ventilated cavitation experiments are displayed in Fig. 1. The experimental setup in Fig. 1(a) includes a high-speed video observation system and a ventilation supply system. The high-speed video of ventilated cavitation, which is composed of the time sequence of ventilated cavitation behaviors, is obtained by a high-speed digital camera (HG-LE, by Redlake) with two dysprosium lamps illuminating the flow field from two different directions to ensure sufficient illumination. The sampling frequency, 3000 frames/s, for the camera is set to achieve and maintain the ideal spatial resolution. The tested cavitator is kept in the viewing area of the camera and installed in the test section by a side pipe that is applied to direct gas. The gas is driven by a compressor that collects and compresses the gas from the environment and is delivered through a flowmeter with a full scale of 1000 L/h. Moreover, the maximum uncertainty in the gas injection coefficient is tested to be ∼2%. Figure 1(b) presents the dimensions of the conical axisymmetric body with side support in the test section and the gas flow trajectory in the body. To further show how the conical axisymmetric body is mounted in the test section, a vertical view on the side support (a stainless-steel pipeline) is drawn in Fig. 1(a). The streamwise distance from the supporting pipeline to the conical body head is 105 mm. The length and diameter of the conical axisymmetric body are 126 and 20 mm, respectively. In addition, the conical axisymmetric body fixed in the middle of the test section is a hollow cylinder with an 8 mm conical head and

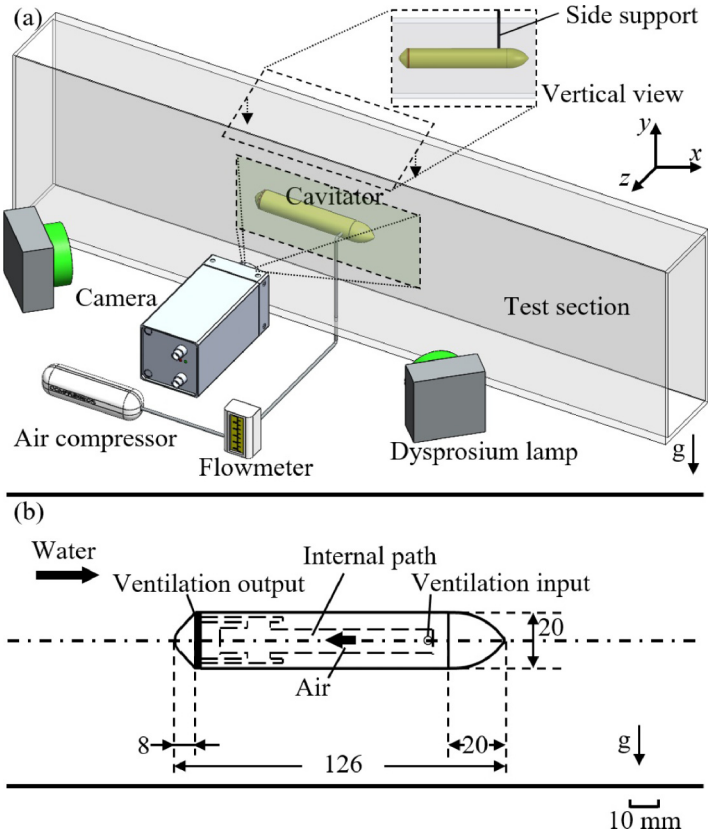


FIG. 1. Schematics of experimental setup and the cavitator. (a) The experimental setup with ventilation system for imaging the ventilation cavity. (b) The test section and the position of the cavitator. All dimensions are in millimeters.

a circumferential seam with a width of 1 mm, allowing the gas to enter the flow field as designed on the axisymmetric body and located 10 mm from the apex. The distance from the apex to the seam is set equal to the radius of the axisymmetric body (10 mm). The seam is formed between the removable head and a hollow cylinder. This design helps us to study the cavitation behavior of different head shapes (e.g., flat plate, sphere, cone) with approximately the same dimension. The gas injected into the conical axisymmetric body is from the ventilation input that is connected to the side pipe. The black arrow in the cavitator indicates the gas flow direction. In this experimental

TABLE I. The flow and ventilation parameters for the experiments.

| Parameters | Symbol (unit) | Range |
|---|---|---|
| Conical body length | $L$ (m) | 0.126 |
| Axisymmetric tested body diameter | $D_n$ (m) | 0.02 |
| Free-stream velocity | $U_\infty$ (m/s) | 4.03–8.08 |
| Ventilation rate | $Q_{\text{in}}$ (L/h) | 100–1000 |
| Froude number based on $D_n$ | $\text{Fr} = U_\infty/\sqrt{gD_n}$ | 9.62–17.07 |
| Reynolds number based on $D_n$ | $\text{Re} = U_\infty D_n/\upsilon$ | 0.84–1.49 ($\times 10^5$) |
| Ventilation coefficient | $C_Q = Q_{\text{in}}/U_\infty D_n^2$ | 0.0086–0.1630 |

study, the ventilation pressure was maintained at 4 atm, and the volumetric velocity of the injected gas varied from 0 to 1000 L/h (0–16.7 SLPM), controlled by the flowmeter. The model of the gas flowmeter is LZB 6 manufactured by Dongtai Dongxing Instrument Factory, China. Relatively, the velocity of the upstream ranges from ∼4 to 8 m/s, and the free stream pressure is fixed at 1 atm. All parameters involved in this paper are presented in Table I. Here, $D_n$ denotes the diameter of the conical axisymmetric body (20 mm), and $\upsilon$ refers to the kinematic viscosity coefficient of water ($1.006 \times 10^{-6}\,\mathrm{m}^2/\mathrm{s}$ at 298 K).

## III. RESULTS

### A. Globe flow patterns

A wide range of conditions and several ventilated flow patterns around a conical axisymmetric body are investigated. It is noteworthy that, in this paper, we neglect the effect of gravity by sufficiently increasing the Fr for simplicity. Therefore, in this paper, we focus on high-Fr cases (Fr $>$ 9.62) to discuss the cavity characteristics. According to experimental observation, the flow patterns are renamed as the FC, the intermittent and transitional cavity (ITC), and the continuous and transparent cavity (CTC) under different Fr and $C_Q$ values, as presented in Fig. 2 (corresponding time sequences are provided in Video 1 in the Supplemental Material [38]). The definition of flow patterns is based on cavity morphology and closure mode, as discussed below.

At low ventilation rates, as shown in Fig. 2(a), FC appears with lots of dense foamy bubbles and unclear gas-water interface around the axisymmetric body surface. The foamy bubbles roll on the front of the conical axisymmetric body, forming a recirculating vortex. The bubbles form small-scale foam shedding, which has been observed in the previous study [33]. Note that $D_C$ is applied to denote the maximum diameter of whole cavity. As the ventilation rate increases, the cavity transits gradually from FC to ITC, as shown in Fig. 2(b). It is observed that foam covers the

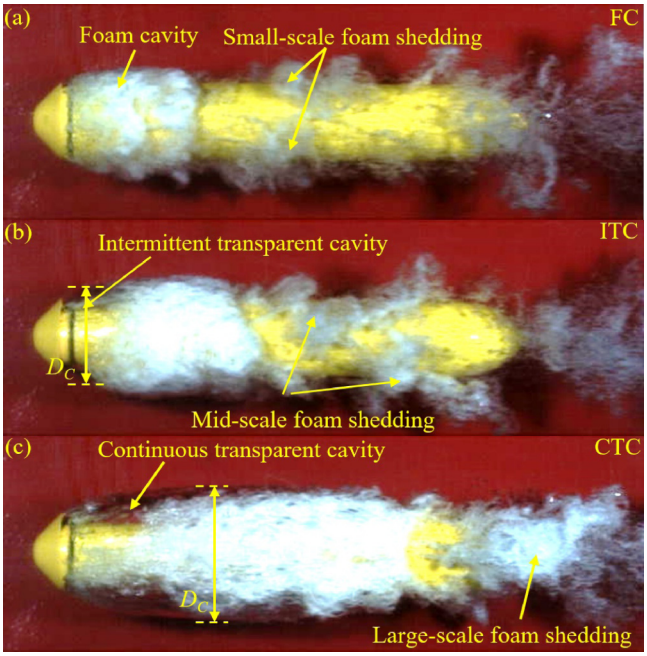


FIG. 2. Side views of the ventilated cavitation observed in the experiments: (a) Foamy cavity (FC) at Fr = 17.07, $C_Q = 0.028$. (b) Intermittent and transitional cavity (ITC) at Fr = 17.07, $C_Q = 0.059$. (c) Continuous and transparent cavity (CTC) at Fr = 14.25, $C_Q = 0.110$.

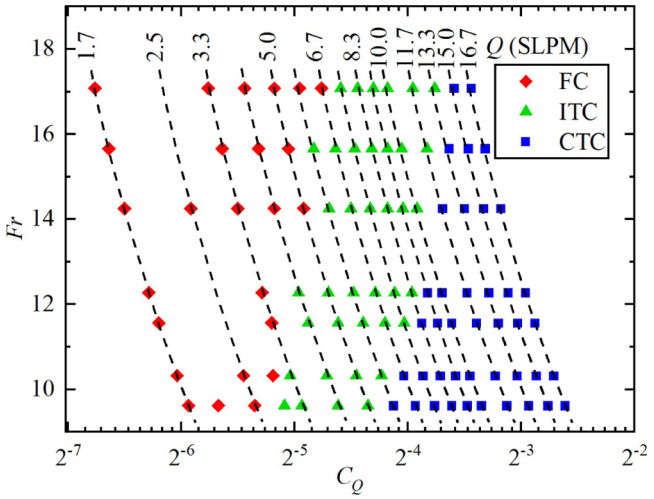


FIG. 3. Globe flow patterns of ventilated cavities around an axisymmetric cavitator.

whole cavity intermittently. Specifically, the recirculating vortex at the rear of the cavity periodically grows back to the front, which leads the intermittency. When the foamy region does not approach the cavity front, a transparent region with a clear gas-water interface is observed at upstream locations of the foamy region. When the foamy region covers the whole cavity, the clear gas-water interface vanishes and the cavity presents a similar flow structure to FC, except that the shedding foam has an increased dimension scale, namely, midscale shedding. As the ventilation rate further increases, the cavity transits to CTC, a continuous transparent cavity presenting a relatively stable gas-water interface which covers the position of $D_C$. Additionally, a recirculating vortex is observed at the rear. Compared with ITC, no gas-water interface broken-up phenomenon but slight fluctuation on the overall structure is observed in CTC. Moreover, large-scale foam shedding is observed in CTC compared with ITC.

The global map of the three typical flow patterns over a wide range of experimental conditions investigated at various Fr and $C_Q$ is established in Fig. 3. As shown, FC denoted by red diamonds is distributed on the left side of the map, while CTC denoted by blue squares lies on the right side. In addition, it is observed from the distribution of these flow patterns that increasing $C_Q$ leads the transition from FC to CTC at a fixed Fr. The regime of FC at high Fr (e.g., Fr = 17.07) is significantly wider than that at low Fr (e.g., Fr = 9.62). The regime of CTC presents the opposite trend. As a comparison, the regime of ITC occupies approximately the same area at different Fr. In addition, as Fr increases, $C_Q$ required for the flow pattern transitions to happen is also increased. To study the formation/transition mechanisms of the flow patterns (i.e., FC, ITC, and CTC), the gas entrainment/leakage models for all flow patterns are established in the next section.

### B. Formation and transition mechanisms

In this subsection, the detailed flow structures for different flow patterns are discussed based on the experimental observation to investigate formation and transition mechanisms. Different from the past works, a topological analysis of mechanisms on gas entrainment and gas leakage is presented below.

As shown in Fig. 4(a) (also presented in Supplemental Material Video 2 [38]), the foamy bubbles roll over around the body surface in the form of a recirculation region. The recirculation region contains a large vortex carrying the dispersed bubbles circulating within, like Qin *et al.* [18] and Sun *et al.* [35]. Figure 4(b) shows a schematic gas entrainment/leakage model for FC. Note that the arrows denote the flow of the gas-water mixture (foam). As the ventilated gas is injected into the

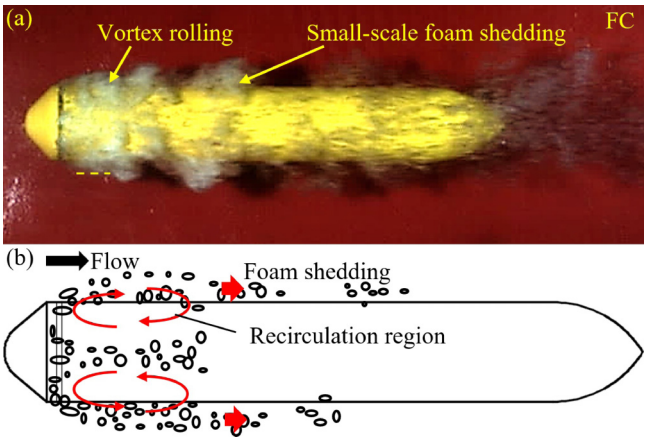


FIG. 4. (a) Experimental observation and (b) schematic illustration of the cavity flow field and bubble dynamics of the foamy cavity (FC) at Fr = 12.27, $C_Q = 0.026$.

water, it breaks into dispersed bubbles which are immediately entrained by the recirculating vortex. Parts of the bubbles are carried downstream by the vortex to form the small-scale foam shedding due to the shear of free stream. Thus, the closure of FC is driven by the recirculating vortex, and the gas leakage of FC is attributed to the small-scale foam shedding. It is reasonable to infer that the volume of gas leakage is related to the size and frequency of the foamy vortex shedding. In FC, weak periodicity in the small-scale foam shedding is observed, indicating distinct high shedding frequency. Furthermore, in FC, as $C_Q$ increases, it is observed that more gas is entrained by the recirculating vortex, and the size of the recirculating vortex is visibly increased. Additionally, more gas sheds downstream to keep the gas volume balance in the cavity. It is reasonable to considered that there is an important positive correlation between the gas leakage and the gas entrained by the recirculating vortex according to Corrsin and Kistler [39] and Meneveau and Sreenivasan [40].

As the ventilation rate further increases, a transparent region is formed at the front of the cavity, and the recirculating vortex appears at the rear of the cavity, as shown in Fig. 5(a), meaning that ITC is developed. In ITC, the transparent cavity is unsteady due to the fluctuation of the recirculating vortex, as presented in Supplemental Material Video 3 [38], which shows the evolution of ITC under the same experimental conditions of Fig. 5. As the recirculating vortex covers the whole cavity, the entrainment of the vortex breaks down the transparency into the dispersion, which is like FC. In addition, parts of the gas in the recirculating vortex are entrained by the free stream to the downstream to form midscale foamy vortex shedding. Figure 5(b) illustrates the gas entrainment in ITC and gas leakage downstream. Note that the hollow arrows denote the gas flow in the transparent region. Specifically, the injected gas is firstly entrained by the internal boundary layer (presented by the green dashed line) inside the transparent region and then moves downstream (enlightened by our previous work Wu *et al.* [23]). When the gas is moving downstream, a portion of the gas is entrained into the reverse flow, which is eventually entrained back into the internal boundary layer at the front of the cavity. In contrast, the rest of the gas is entrained into the recirculating vortex with midscale foam shedding. Considering ITC can be maintained under fixed experimental conditions, the total volume of gas leakage would be equal to the total ventilation during a whole period of the unsteady behaviors, as presented in Liu *et al.* [33]. Like FC, the volume of the gas leakage is related to the frequency and size of foamy vortex shedding. However, the shedding frequency of ITC is significantly reduced compared with that of FC. Meanwhile, the size of the shedding vortex is increased. The reason is twofold. First, the reduction of the shedding frequency is possibly caused by the reduced inverse pressure gradient with increasing ventilation rate, according to Lv *et al.* [30] and Sun *et al.* [36]. Second, the increased size of the shedding is possibly because of the increased size

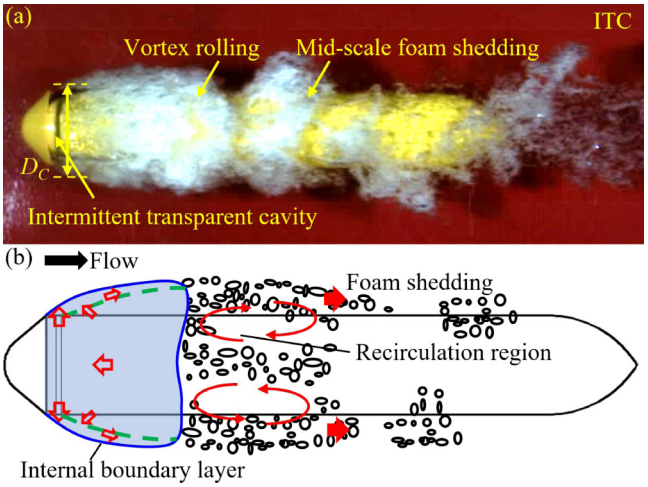


FIG. 5. (a) Experimental observation and (b) schematic illustration of the cavity flow field and bubble dynamics of the intermittent and transitional cavity (ITC) at Fr = 12.27 and $C_Q = 0.051$.

of the recirculating vortex. According to Supplemental Material Video 3 [38], the periodic vortex shedding behind the cavity shares similar characteristics to the van Karman vortex street around a cylinder [41–43] and a hydrofoil [44]. For the van Karman vortex street, the Reynolds number ($\mathrm{Re} = UD/v$) is positively correlated with the size of the vortex shedding [45]. Therefore, for the ventilated cavity in this case, the size of the shedding can be inferred to be positively correlated to the size of the recirculating vortex. Because of this twofold reason, the reduced shedding frequency is compensated by the increased size of the shedding to balance the gas injection and leakage.

As $C_Q$ is further increased, the length of the transparent region is increased significantly, and the flow pattern is transformed into CTC, as shown in Fig. 6(a). CTC consists of a continuous transparent cavity with a clear gas-water interface at the front and a recirculating vortex at the rear,

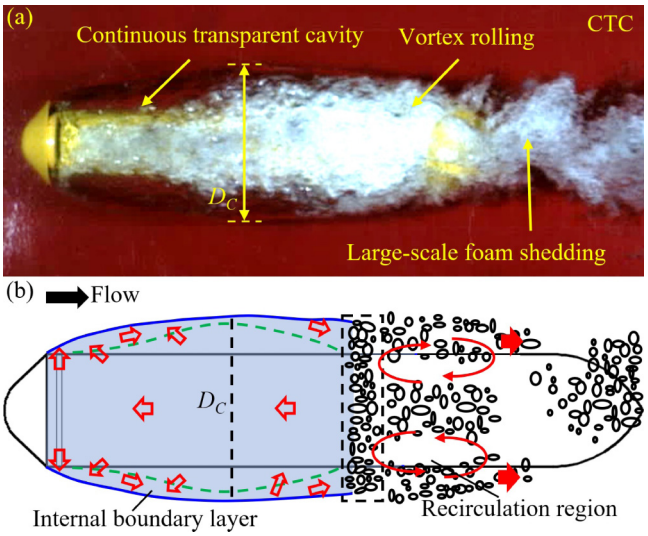


FIG. 6. (a) Experimental observation and (b) schematic illustration of the cavity flow field and bubble dynamics of the continuous and transparent cavity (CTC) at Fr = 12.27 and $C_Q = 0.102$.

as presented in Supplemental Material Video 4 [38]. The differences between CTC and ITC are also divided into two aspects. First, the continuous transparent region in CTC is relatively steady and covers the position of $D_C$. Second, the size of the recirculating vortex in CTC is further increased compared with ITC. In CTC, considering the recirculating vortex cannot grow upstream to reach the front of the axisymmetric body, the clear gas-water interface is approximately stable. Figure 6(b) further shows the gas entrainment and leakage of CTC. Note that the position of $D_C$ is in the transparent region. As the gas is injected into the flow field, it is immediately entrained into the internal boundary layer like ITC. However, parts of the gas are entrained across the green dashed line into the reversed flow behind the position of $D_C$. Moreover, the end of the transparent region would be entirely occupied by the downstream moving internal boundary layer (like the vortex tube in Wu *et al.* [23]). Then gas flow in the internal boundary layer is entrained into the recirculating vortex. Finally, large-scale foam shedding is formed under the shear of the free stream. Interestingly, according to our observation, a significant increase in cavity length is observed during the transition from ITC to CTC under a slight increase of $C_Q$, which could be considered the ventilated hysteresis, as presented by Kawakami and Arndt [26]. However, different from Kawakami and Arndt [26], who observed the free-standing supercavity right after the hysteresis, the CTC is observed in our experiments after the ventilated hysteresis instead of the supercavity. This discrepancy of flow patterns can be explained briefly as follows: For CTC, the internal boundary layer occupies the transparent region at the cavity rear before the recirculating vortex. Due to the shear of the free stream, the gas entrained inside the boundary layer could be excluded from the cavity in the form of a vortex tube surrounding the body, even if the recirculating vortex does not present (like the free-standing supercavity). However, the recirculating vortex still presents in our study due to the interaction between the gas-water interface and the axisymmetric body surface. A detailed analysis of the recirculating vortex presence in CTC will be presented in Sec. III C.

The analysis for different cavity flow patterns is briefly summarized. First, under fixed Fr, three flow patterns, FC, ITC, and CTC, are obtained successively as $C_Q$ increases. Second, for all flow patterns, gas leakage is related with the size and frequency of the foam shedding. Specifically, as the ventilation rate increases, the mean size of shedding foam gradually increases but with reduced shedding frequency. For each flow pattern, the gas injection is always balanced by the corresponding size and frequency of the foam shedding.

To present the effect of Fr on the transitions of flow patterns, the $C_Q$-Fr curves as well as the boundary lines (BLs) for FC-to-ITC (BL 1) and ITC-to-CTC (BL 2) transitions are displayed in Fig. 7. The $C_Q$-Fr curves demarcating neighboring flow pattern regimes (e.g., between FC and ITC, and ITC and CTC) can be obtained using the least square fitting of the mean values of the data points located near the BLs between the two regimes. It is observed that the required $C_Q$ for the transition from FC to ITC increases from 0.027 to 0.040 as Fr increases from 9.62 to 17.07. Meanwhile, the required $C_Q$ for the transition from ITC to CTC increases from 0.053 to 0.073 as Fr increases from 9.62 to 17.07. In other words, as Fr increases, the required $C_Q$ for each transition is correspondingly increased. The increased $C_Q$ requirement can be accounted for by the increased Fr enhancing gas leakage at the cavity rear [18,46]. According to Spurk [25], Wu *et al.* [23], and Lv *et al.* [30], larger gas leakage is caused by stronger flow separation at the cavity rear due to increased adverse pressure gradient (APG) under higher Fr.

### C. Ventilation hysteresis from ITC to CTC

Ventilation hysteresis is considered the nonlinear relationship [47] between ventilation rate $Q_{in}$ and the length of the transparent cavity when the supercavity is forming or collapsing. Particularly during the cavity formation process, a slight increase of the ventilation rate could lead the flow pattern to transform from FC to a supercavity with significant increase of length of the transparent cavity. Similarly, during the cavity collapsing process, a slight reduction of the ventilation rate could cause the significant decrease of length of the transparent cavity and eventually the complete collapse. More importantly, the critical ventilation rate required to form the cavity is significantly

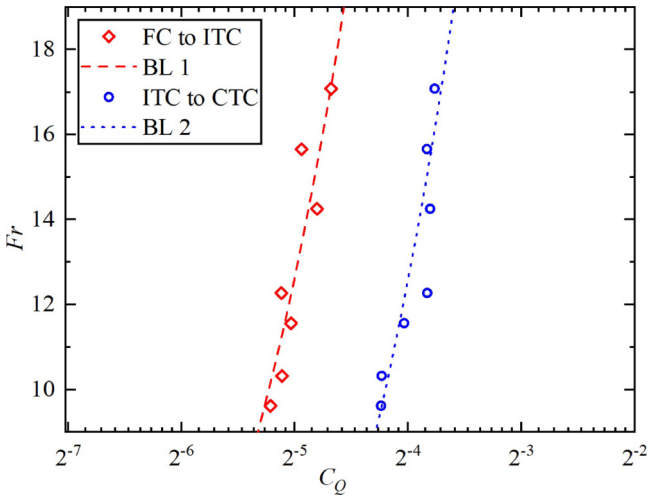


FIG. 7. The boundary lines separating contiguous flow patterns.

greater than that needed to destroy the cavity [26]. In this paper, the ventilation hysteresis that happens during the cavity formation process is the main focus.

The ventilation hysteresis from ITC to CTC is quantitatively discussed in this subsection, with the mechanism explained in detail. Specifically, it is observed in our experiments that the length of an ITC increases significantly to achieve CTC once the ventilation rate slightly exceeds the upper limit of ITC. Additionally, as the transition from ITC to CTC happens, the position of the maximum diameter is enclosed by a markedly increased continuous transparent cavity rather than staying between the transparent region and the recirculating region. This ventilated hysteresis is like the study presented by Kawakami and Arndt [26] for a cavitator with the thin struts behind. However, different from their study that a supercavity is obtained right after the hysteresis without the RJ closure, the flow patterns of CTC contain an apparent recirculation region at the cavity rear. To provide a reasonable explanation of the hysteresis presented in this paper, the cavity geometry is closely examined, and a quantitative model is developed to demonstrate the gas entrainment and leakage of the cavity during hysteresis. Based on the theoretical model, the physical mechanism of ventilation hysteresis from ITC and CTC is elaborated.

To quantify the change of cavity geometrical shape during hysteresis, two parameters, the cavity length ($L_C$) and diameter ($D_C$), are graphically defined in Fig. 7, where the representative instantaneous flow patterns of ITC and CTC are presented in Figs. 8(a) and 8(b), respectively. Considering the instantaneous variation of the shape on cavitation, to indicate the time-averaged change during the transition, $L_C$ and $D_C$ are the mean values of the multiple metering (averaged using 50 measurement frame sequences), denoting the average length and maximum diameter of the transparent region, respectively. As presented in Figs. 8(a) and 8(b), $D_C$ of an ITC cavity is at the most downstream location of the transparent cavity region due to its diverging geometry, while $D_C$ of a CTC cavity is marked out in the middle of the transparent region. To help the definition of the proposed cavitation flow model, the averaged radius ($R_C$), defined as half of $D_C$, is employed in the discussion later. Additionally, as shown in Fig. 8(c), the foam shedding, named by current shedding, is marked with a yellow circle and the time marked as $t = t_0$. In Fig. 8(d), the foam shedding marked in at $t = t_0$ is remarked as previous shedding with $t = t_1$. In addition, the time difference between Figs. 8(c) and 8(d) can be obtained by $\Delta t = t_1 - t_0$. In this paper, for each ITC, the mean time difference $\Delta t_{\text{ave}}$ is determined by the 20 measurements on $\Delta t$. Then the frequency of foam shedding is calculated by $f = 1/\Delta t_{\text{ave}}$. Likewise, $f$ is also employed in the model discussed later.

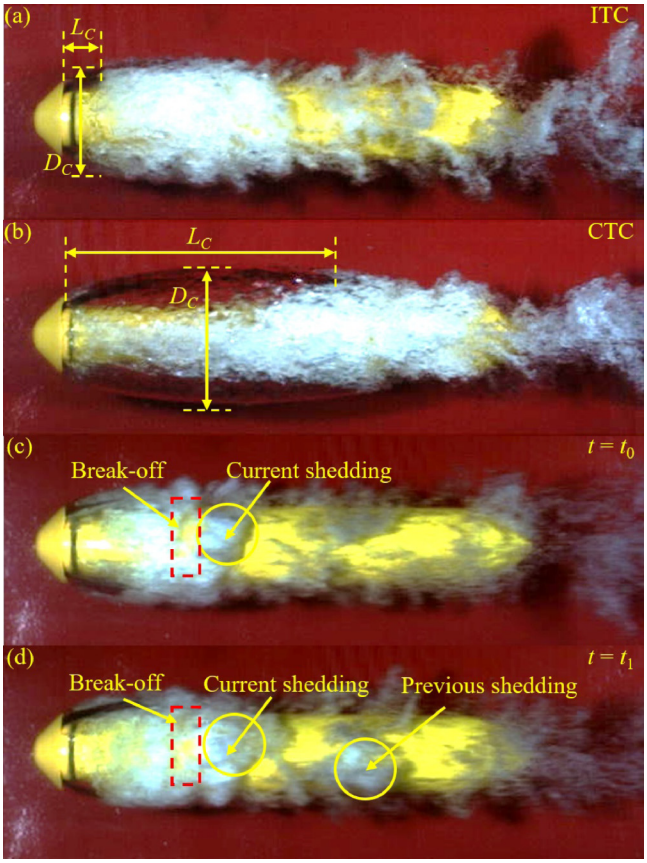


FIG. 8. Schematic of dimension and shedding frequency measurements. The cavity length ($L_c$) and maximum diameter ($D_c$) of (a) the intermittent and transitional cavity (ITC) and (b) the continuous and transparent cavity (CTC). Wake bubble break-off and shedding tracking at (c) $t = t_0$ and (d) $t = t_1$.

The variation of $L_C$ and $R_C$ with $C_Q$ under different Fr is presented in Fig. 9. Particularly in the gray shadow regions, $L_C$ shapely increases with only slight increment of $C_Q$. When $C_Q$ increases from $2^{-5}$ to $2^{-3}$, the change of $L_C$ is significant enough with severalfold increase, while $R_C$ only grows slightly. This observation proves quantitively that the prominent changes in morphology happen because of the ventilated hysteresis on the conical axisymmetric body. For instance, under Fr = 12.27, $L_C$ increases by $> 4$ times (from 10.62 to 45.60 mm) as $C_Q$ slightly increases from 0.064 to 0.070. After the sudden length jump, as $C_Q$ further increases, $L_C$ is also observed with gradual increase with reduced slope. On the contrary, the variation of $R_C$ does not experience the obvious hysteresis. For the case of Fr = 12.27, $R_C$ smoothly increases from 13.08 to 17.86 mm as $C_Q$ increases from 0.032 to 0.128. However, it is observed from Fig. 9 that $R_C$ in the different Fr cases converges to approximately the same value (i.e., 17.86 mm) as $C_Q$ becomes sufficiently large (at the maximum value), which manifests that the maximum radius of ventilated cavitation is weakly correlated with Fr. This observation is in accordance with the typical model of the ventilated hysteresis studied by Kawakami and Arndt [26].

To quantify the gas leakage with cavity morphology during the hysteresis, a 3D theoretical flow model is established for the ITC cavity, as illustrated in Fig. 10. Since the ITC cavity has its maximum radius $R_c$ located between the transparent region and recirculating foam, the measurement and quantitative relationship of gas shedding, we can assume that the periodical foam shedding starts

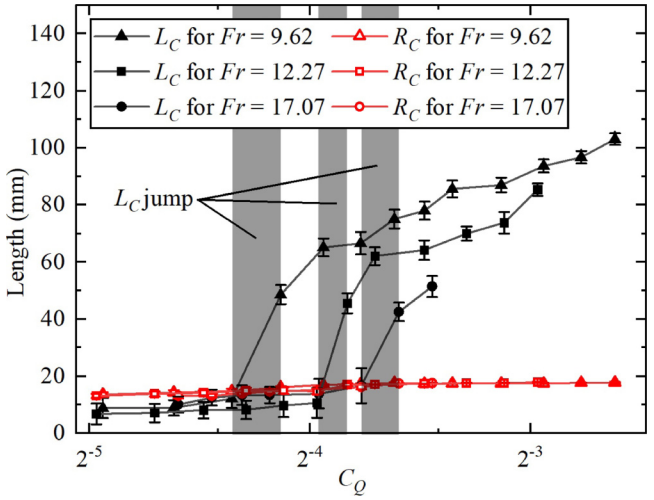


FIG. 9. The variation of cavity length ($L_C$) and maximum radius ($R_C$) with different ventilation $C_Q$ under Fr = 9.62, 12.27, and 14.22.

from locations of $R_C$ in the form of a vortex ring surrounding the conical axisymmetric body. Hence, the sectional area of the vortex ring is expressed by $\pi(R_C - R_n)^2/4$, where $R_n$ denotes the radius of the cavitator, as shown in the front view in Fig. 10(a). The length of the central axis of the vortex ring can be estimated by $\pi(R_C + R_n)$, as presented in the end view in Fig. 10(b). Consequently, the volume of each vortex ring can be calculated by $\pi^2(R_C - R_n)^2(R_C + R_n)/4$. Eventually, the mathematical relationship between gas leakage $Q_{\text{out}}$ and vortex ring volume can be expressed in the form below:

$$Q_{\text{out}} = \frac{Kf\pi^2(R_C - R_n)^2(R_C + R_n)}{4},$$

where $K$ is an empirical value representing the comprehensive impacts of void fraction and turbulent breakup of the vortex ring. Practically, $K$ should be less than unity (unity = 1) since the shedding vortex ring entrains the gas-water mixture rather than pure gas, and the turbulence at the cavity rear intermittently break up the vortex rings into filaments before any complete rings can be formed. It can be observed in our experiments that almost all bubbles, filaments, and air pockets are entrained by the vortex rings, broken up by the turbulence, and then carried downstream by the free water stream. Hence, it is not likely to observe noticeable azimuthal shedding modes under our tested conditions. Here, $f$ is the shedding frequency of vortex rings. The shedding frequency $f$ can be

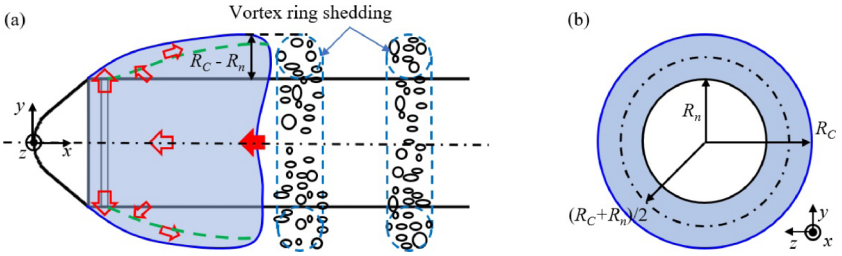


FIG. 10. (a)The schematic of the vortex ring shedding model applied in intermittent and transitional cavities (ITCs). (b)The shed vortex rings have an averaged cross-sectional radius of $(R_C - R_n)/2$ and a central axis length of $\pi(R_C + R_n)$.

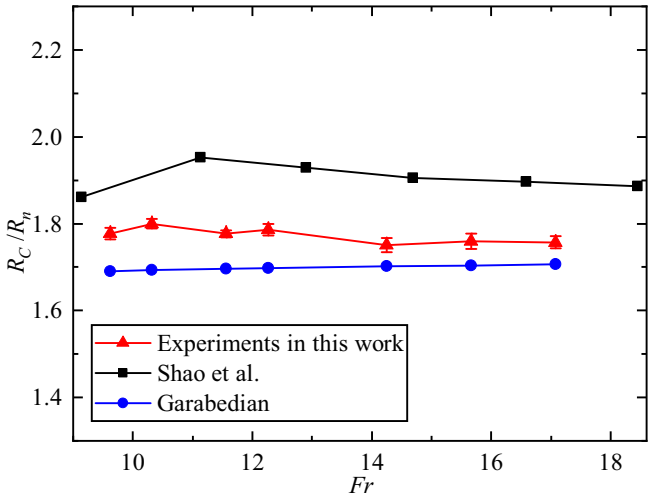


FIG. 11. Normalized maximum radius $R_C/R_n$ of the cavity developed on the conical cavitator over the range of tested Fr cases. All data are obtained from the cavity under maximum ventilation coefficient. The error bars shown here correspond to the standard deviation of the 50 independent measurements. The results by Shao *et al.* [32] and Garabedian [49] are presented under the same flow conditions as ours for comparison purposes.

nondimensionalized using the Strouhal number (St):

$$\mathrm{St} = \frac{f(R_C - R_n)}{U_\infty},$$

where the characteristic length (i.e., $R_C - R_n$) is selected as the cross-sectional dimension of the shedding vortex ring according to Dular and Bachert [48]. The gas leakage can then be modified as

$$Q_{\mathrm{out}} = \frac{K\mathrm{St}U_\infty \pi^2 \left(R_C^2 - R_n^2\right)}{4}. \tag{1}$$

Since the ventilation coefficient $C_Q$ is expressed by $C_Q = Q_{\mathrm{in}}/(U_\infty D_n^2) = Q_{\mathrm{in}}/(4U_\infty R_n^2)$, and for ITC $Q_{\mathrm{in}} = Q_{\mathrm{out}}$ can be obtained due to the cavity volume balance, it is further written as

$$C_Q = \frac{K\mathrm{St}\pi^2\left[\left(\frac{R_C}{R_n}\right)^2 - 1\right]}{16}. \tag{2}$$

As revealed by Eq. (2), the gas leakage of ITC is correlated with the shedding periodicity (represented by St) and cavity geometry (represented by $R_C/R_n$), which are decided by experimental measurements. Therefore, to validate the effectiveness of Eq. (2), the rationality of each term on the right-hand side of Eq. (2) must be proved in advance.

Figure 11 compares the cavity geometry parameter ($R_C/R_n$) measured in our experiments and a couple of past studies. For brevity, the $R_C/R_n$ values are compared for fully developed cavities with sufficiently large $C_Q$ (e.g., CTC). As shown in Fig. 10, the experimental results of $R_C/R_n$ in this paper are slightly reduced by ~0.1 compared with those from Shao *et al.* [32] for cases with different Fr. This discrepancy can be primarily attributed to different cavitator shapes and blockage of the water tunnel, as explained in Karn *et al.* [5]. Additionally, Garabedian [49] calculated $R_C/R_n$ using an empirical formulation $R_C/R_n = \sqrt{C_{D_0}(1+\sigma_\infty)/\sigma_\infty}$ (marked in blue), where $C_{D_0}$ denotes the drag coefficient extrapolated from the experimental data assembled by May [50] and Lee *et al.* [51], and $\sigma_\infty$ is the unbounded cavitation number estimated by $\sigma_\infty = 0.5 \cdot [(0.8509 - 1.472B^{-0.3755})\mathrm{Fr}^{-4/3} + 3.885B^{-1.276}]$ according to Zou *et al.* [52] and Lee *et al.* [51]. In $\sigma_\infty$ calculation, $B = D_T/D_n = 6.5$ denotes the blockage ratio, where $D_T$ is the

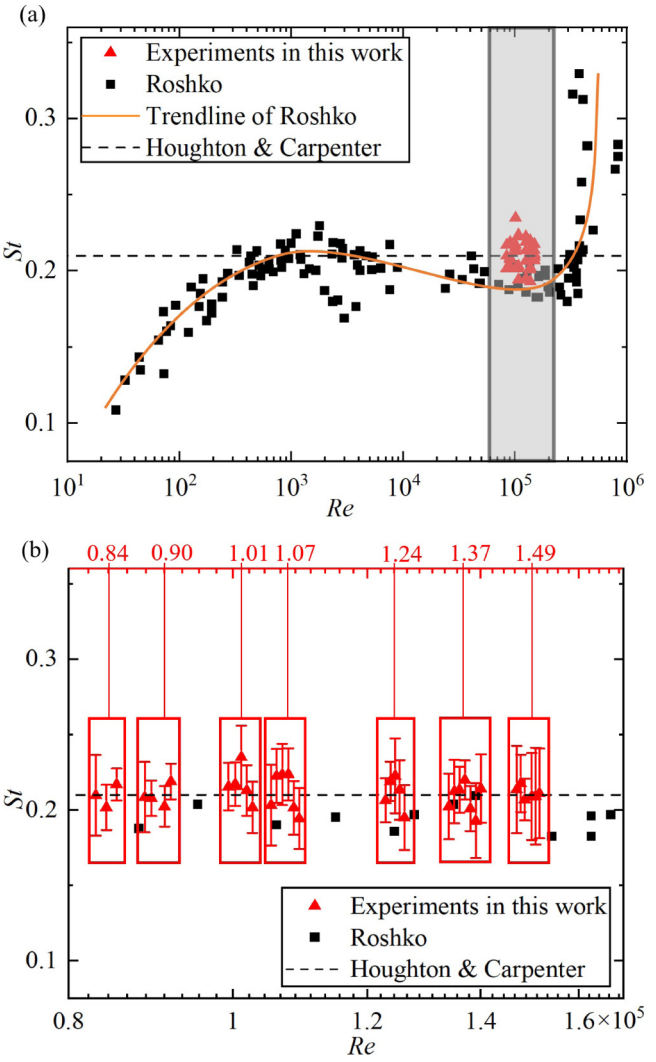


FIG. 12. The Strouhal number distribution under (a) a global and (b) a specific range of Re for intermittent and transitional cavities (ITCs) in our experiments. For comparison, all data marked by black squares are from Roshko [54], and the dashed line, 0.21, corresponds to conclusion from Houghton and Carpenter [55].

hydraulic diameter of the closed-wall water tunnel in this paper (0.13 m). The estimated $R_C/R_n$ values by Garabedian [49] are slightly lower than our experimental results. This underestimation can be primarily attributed to the variation of test section pressure along the cavity span due to the cavity-induced blockage and friction loss, which is not fully addressed by the semiempirical formulation based on potential theory [32]. Additionally, it can be observed from all presented studies that the values of $R_C/R_n$ are only weakly dependent on Fr once the cavity is substantially developed. Similar observations are also provided by other studies like Karn *et al.* [5] and Jiang *et al.* [53]. In short, it is concluded that both the values and the trend of $R_C/R_n$ measured in this paper present reliable accuracy.

Figure 12 shows the St comparison between our experiments and past studies in a global range of Reynolds numbers Re of the incoming flow. Specifically, the black squares are obtained from Roshko [54], representing the St calculated from the periodic shedding of the von Karman vortex

street, which is generated from a cylinder wake flow. As shown in Fig. 12(a), in the range of $5 \times 10^2 < \mathrm{Re} < 5 \times 10^5$, the data distribution shows that the St values are concentrated ~0.2. Additionally, Houghton and Carpenter [55] provided a similar conclusion that the St of vortex shedding in the cylinder wake is about a constant (0.21) under $\mathrm{Re} > 1000$, denoted by the dashed line. Similarly, the calculated St values from our experiments, denoted by red triangles, are also concentrated around $\mathrm{St} = 0.21$. To better demonstrate the St distribution under the tested Re range of our work, Fig. 12(b) expands the shaded region from Fig. 12(a) for clear illustration. As shown in Fig. 12(b), all boxed St data points (red triangles) are measured under the same Re (due to the same Fr) with different ventilation coefficient $C_Q$. To avoid overlap, the data points are arranged with increasing $C_Q$ in each box, and the corresponding Re values are marked out on the upper $x$ axis. Within the tested range of $0.84 \times 10^5 \leqslant \mathrm{Re} \leqslant 1.49 \times 10^5$, the St values are distributed ~0.21 with an error bar <0.06. The error bar is calculated using the standard deviation obtained from the 50 measurements of shedding frequency and vortex diameter. The distribution of calculated St in this paper verifies the hypothesis that the vortex shedding of ventilated cavities and cylinder wake flow share similar periodicities. The results demonstrate that it is reasonable to set St as a constant (0.21) in further validation steps of the gas leakage model expressed by Eq. (2).

Since the above analysis of Figs. 11 and 12 proves that both $R_C/R_n$ and St are reasonably decided by our measurements, the parameter $K$ can be calculated in Eq. (2) under different flow conditions (i.e., different Fr and $C_Q$ combinations), as shown in Fig. 13(a). By examining the projections of $K$ on the Fr axis (green marker) and $C_Q$ axis (blue marker), it is very interesting to observe that the values of $K$ are distributed $\sim 0.36 \pm 0.08$. This observation provides critical evidence to support the gas leakage model of ITC represented by Eq. (2). Specifically, under the studied experimental conditions in this paper (i.e., $9.62 \leqslant \mathrm{Fr} \leqslant 17.07$, $0.032 \leqslant C_Q \leqslant 0.128$), the parameter $K$ can be approximately regarded as a constant, which indicates the comprehensive impacts of the void fraction, and turbulent breakup of vortex rings keeps invariant with Fr and $C_Q$ in our experiments. In addition, as observed from Fig. 12, St is also independent from Fr and $C_Q$ and can be treated as a constant (0.21). Hence, the gas leakage $C_Q$ of ITC is monotonically determined by the radius ratio ($R_C/R_n$). As the cavity radius $R_C$ reaches the maximum, the ITC reaches a critical status with maximum gas leakage $C_Q$. Further slightly increasing ventilation rate would break up the gas input-leakage balance and lead to the transition from ITC to CTC, which is sorted as a type of ventilation hysteresis by Kawakami and Arndt [26]. The critical $C_Q$ for such a transition is calculated by substituting the maximum $R_C$ obtained from Fig. 9 into Eq. (2). Figure 13(b) presents the calculated critical $C_Q$ values superimposed into the measured flow pattern map (partially cropped from Fig. 3) under different Fr cases. As presented in Fig. 13(b), the locations of calculated critical $C_Q$ are overall in agreement with the experimental observation for all tested Fr cases, which further validates our gas leakage model. Additionally, it is observed from Fig. 13(b) that the error bar of critical $C_Q$ presents an increasing trend as Fr grows since both St and $R_C$ measurements experience increasing uncertainty caused by enhanced wake flow turbulence. During the transition from ITC to CTC, the cavity diameter at closure starts to decrease, leading to a shrinking cross-sectional area and reduced volume of the shedding vortex rings in our gas leakage model. Hence, the gas leakage remains lower than the ventilation input, and the cavity length quickly grows until a quasi-ellipsoid cavity shape (i.e., CTC) is obtained, as shown in Fig. 8(b).

For a CTC, the gas leakage model of vortex ring shedding is no longer applicable since the downstream moving cavity internal boundary layer merges and occupies the whole cavity at the rear, which would be automatically shed without being entrained by the recirculating vortex. Past studies on free-standing cavities or cavities with a thin strut inside [5,32] also observed a similar internal boundary layer leaving the cavity body. Different from our observation on CTCs, the recirculating vortex shedding (a typical pattern of flow separation) vanishes in their CTCs. Instead, they observed the TV tubes at the rear formed by the merging internal boundary layer, and supercavities are achieved. Since the primary instrumentation difference between their and our experiments is the cavitator shape, it is reasonable to deduce that the discrepancy of closure modes is caused by the interaction between the internal boundary layer and the cavitator surface.

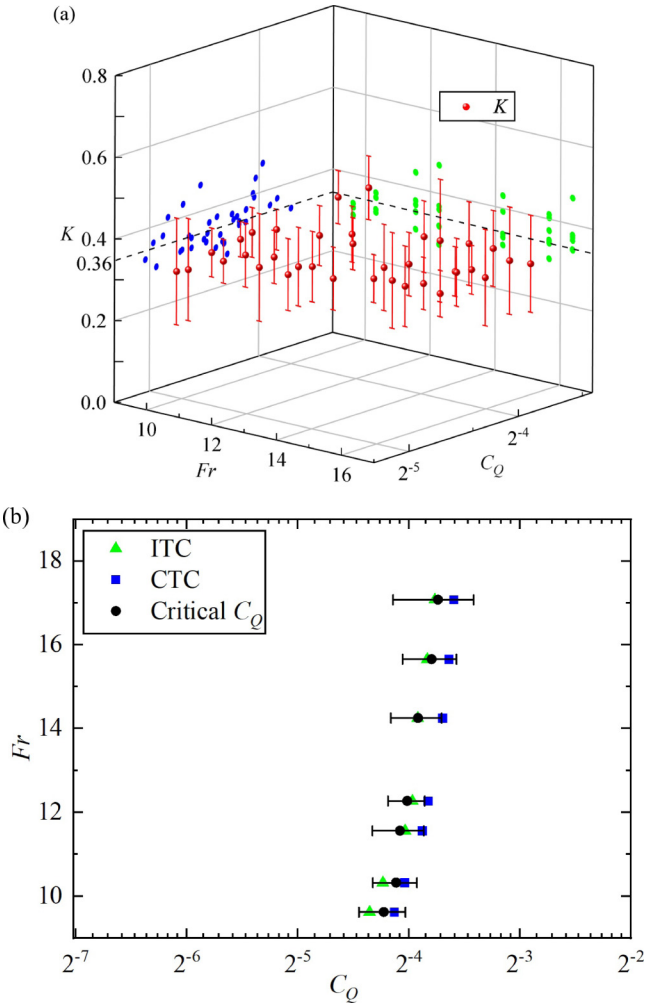


FIG. 13. (a) The distribution of parameter $K$ calculated on intermittent and transitional cavities (ITCs), with projections on Fr and $C_Q$ axes for clear observation of $K$ values. The dashed lines mark out the averaged $K$ (0.36). (b) The estimated critical $C_Q$ from Eq. (2) by substituting the largest $R_C/R_n$ under different Fr cases.

To explain the closure mode discrepancy between the CTCs observed in this paper and the supercavities achieved in previous studies, here, we provide a mechanism to explain the observation, as illustrated in Fig. 14. After the ventilation hysteresis, the CTC on the conical axisymmetric body is seeded with a large ventilation rate, but we still observe recirculating vortex closure with intermittent foam shedding, like FC and ITC [Fig. 14(a)]. On the contrary, the free-standing supercavity with a large ventilation rate has the vortex tube closure [Fig. 14(b)] observed by past works, in which the gas leaves the cavity from the tube without noticeable foam shedding. Since Wu *et al.* [23] have proved that the foam shedding is originated from the water flow separation under large APG which impinges the gas-water interface, it can be reasonably inferred that the CTC should have larger APG than the free-standing supercavity does due to the presence of a large solid body inside the cavity.

An estimation of APG for both cavities is provided to validate our deduction. As shown in the Fig. 14(a), point $A_1$ denotes the point located in the potential water flow at maximum diameter $D_C$, which is right above the boundary layer formed by the gas-water interface. Since the thickness

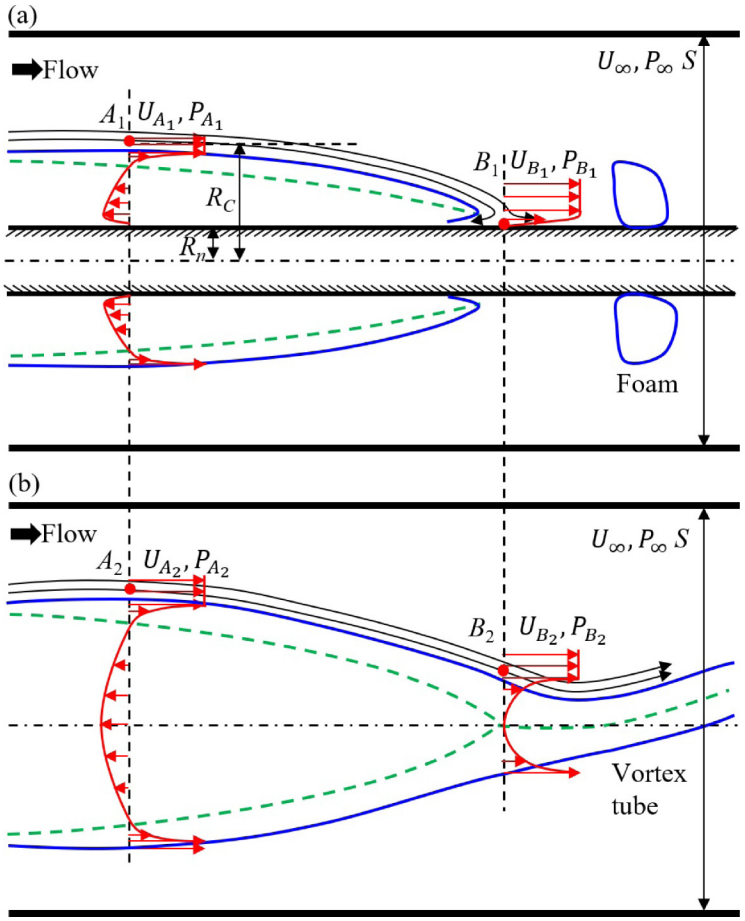


FIG. 14. Schematic of gas flow inside and water flow surrounding (a) the continuous and transparent cavity (CTC) formed on the conical axisymmetric cavitator and (b) the free-standing supercavity formed after a backward-facing strut from Wu *et al.* [23]. Points $A_1$ and $A_2$ are located at the potential water flow close to the gas-water interface. Points $B_1$ and $B_2$ are on the same streamline as $A_1$ and $A_2$, respectively.

of the boundary layer at the water side is typically negligible, the distance from $A_1$ to the cavity axis is approximately $R_C$. The streamline through point $A_1$ intersects the conical cavitator body at point $B_1$, so point $B_1$ is the stagnation point where velocity is zero due the influence of the solid surface. We also define $S$ as the cross-sectional area of the water tunnel and $P_\infty$ as the free stream pressure. By applying the flow continuity equation and assuming the potential water flow has uniform velocity at the same streamwise location, the water velocity at $A_1$, $U_{A_1}$, can be estimated as $U_{A_1} = U_\infty S/(S - \pi R_C^2)$. Additionally, according to the Bernoulli equation, the pressure at $A_1$, $P_{A_1}$, can be estimated by $P_{A_1} = P_\infty + 0.5\rho(U_\infty^2 - U_{A_1}^2)$, where $\rho$ denotes the water density. As for the stagnation point $B_1$, the pressure $P_{B_1}$ is calculated as $P_{B_1} = P_\infty + 0.5\rho U_\infty^2$. Therefore, the APG of the CTC can be calculated by

$$\Delta P_{\mathrm{CTC}} = P_{B_1} - P_{A_1} = 0.5\rho U_\infty^2 \frac{S^2}{\left(S - \pi R_C^2\right)^2}. \tag{3}$$

On the other hand, for a free-standing supercavity formed with same free stream conditions, we define point $A_2$ in the same way as $A_1$, so $U_{A_2} = U_{A_1}$ and $P_{A_2} = P_{A_1}$. Additionally, point $B_1$ is set

at the cavity rear in the same streamline as $A_1$. Since the potential water flow does not impinge the vortex tube at the rear (proved by intact tube structure), $B_2$ would be located right above the vortex tube. Because the vortex tube diameter is typically a few millimeters, much smaller than the water tunnel dimension, we could neglect the blockage effect of the tube and set $U_{B_1} \approx U_\infty$ and $P_{B_1} \approx P_\infty$. Hence, the APG of the supercavity is expressed by

$$\Delta P_{\mathrm{SC}} = P_{B_2} - P_{A_2} = 0.5\rho U_\infty^2 \left[ \frac{S^2}{\left(S - \pi R_C^2\right)^2} - 1 \right]. \tag{4}$$

The ratio between $\Delta P_{\mathrm{CTC}}$ and $\Delta P_{\mathrm{SC}}$ is therefore

$$\frac{\Delta P_{\mathrm{CTC}}}{\Delta P_{\mathrm{SC}}} = \frac{\frac{S^2}{\left(S-\pi R_C^2\right)^2}}{\frac{S^2}{\left(S-\pi R_C^2\right)^2} - 1}. \tag{5}$$

It is very interesting to observe from Eq. (5) that the ratio $\Delta P_{\mathrm{CTC}}/\Delta P_{\mathrm{SC}}$ can be uniquely decided by the geometry parameters of the cavity and water tunnel and independent from flow velocity and pressure. Practically, in our experiments, the water tunnel cross-section area is calculated as $S = 0.19 \times 0.07 = 0.0133\,\mathrm{m}^2$, and the cavity maximum radius is approximately $R_C \approx 0.018\,\mathrm{m}$ (estimated from Fig. 11). Therefore, by substituting $S$ and $R_C$ into Eq. (5), we find $\Delta P_{\mathrm{CTC}}/\Delta P_{\mathrm{SC}} = 6.8$ under the experimental conditions in this paper (i.e., $9.62 \leqslant \mathrm{Fr} \leqslant 17.07$, and $Q_{\mathrm{in}} = 1000\,\mathrm{L/h}$). Such large pressure variation is the primary reason for different flow patterns at the cavity closure. It is noteworthy to mention that the above quantitative estimation is applicable under sufficiently high Fr so that the gravity effects to the cavity geometry are neglected. Otherwise, for low Fr cases, the gravity leads to an upwarped cavity in which the internal boundary layer merges above the cavitator body. In that case, the vortex tube closure would be observed instead of recirculating foam shedding for CTCs. Furthermore, it is interesting to discuss if a free-standing supercavity that encloses the whole cavitator body would be developed from CTC under higher Fr with sufficient $C_Q$. According to the previous work [21], the half-length of a ventilated supercavity $L_k$ can be estimated by $L_k = (1.92{-}3\sigma)R_n/\sigma$. In this paper, the length of the axisymmetric body is ~12 times $R_n$. Hence, to form a free-standing supercavity, a cavity half-length of $L_k/R_n > 6$ should be met. Correspondingly, the cavitation number $\sigma$ is calculated to be <0.213. However, according to the unbounded cavitation number calculation $\sigma_\infty = 0.5[(0.85{-}1.472B^{-0.3755})\mathrm{Fr}^{-4/3} + 3.885B^{-1.276}]$ by Ref. [50] and $\sigma = 2\sigma_\infty$ by Ref. [49], the minimum of $\sigma$ in the tested water tunnel is ~0.358 under infinite Fr. Hence, it seems not quite possible that the free-standing supercavity entirely enclosing our tested body can be formed from CTC. Nevertheless, this conclusion cannot be confirmed until a test run is performed under higher Fr and larger $C_Q$, which is currently beyond our hardware limit.

Finally, we would like to point out some limitations of our current study, and the corresponding cautions required in our experiments are presented as suggestions for future investigations.

First and foremost, direct photography using the high-speed digital camera in the current experiments constrains us from obtaining the detailed flow structure inside the transparent region. Specifically, in this paper, the detailed flow structure inside the transparent region is inferred from past experimental and numerical studies [23,30], which makes it difficult to directly validate our inference about gas leakage and closure mode mechanisms. This limitation can be addressed by seeding particles into the ventilated cavity and using lasers for particle image velocimetry (PIV) illumination. This approach requires significant modification to the cavitator structure and the water tunnel instrumental setup. Additionally, the laser reflection on the cavitator body needs to be sufficiently reduced to avoid interference on the scattering signal of seeding particles.

Second, the discussion on gas entrainment and leakage is mainly involved with the experimental pictures recorded from the front view, which may cause insufficient consideration of the ventilated cavity flow behind the conical axisymmetric body. Moreover, because the conical axisymmetric body is fixed in the test section of the water trunnel with the side support, the cavity structure behind the body is probably disturbed with the support strut, which may influence the gas entrainment and

leakage of the ventilated cavity flow. This limitation can be addressed by changing the support mode from the side support to the tail support in future works.

Third, we currently observe the physical dimension of the foam shedding by eyeball check on the cavity photos. A more rigid optical method such as the digital holography may be induced in future works to precisely determine the bubble size and distribution in the foam, which is helpful to decide the exact dimension of the shedding vortex rings, and provide more solid evidence to validate the gas leakage model developed in this paper.

Fourth, our current measurements cannot derive the pressure field over the flow field. Therefore, it is difficult for us to accurately estimate the static pressure in the flow field and the APG in the water flow around the gas-water interface with the experimental pictures of ventilated cavities. Such pressure field measurements may be achieved by the detailed velocity field data if high-fidelity acceleration field can be extracted from time-resolved planar PIV measurements as introduced in Liu and Katz [56].

## IV. CONCLUSION AND DISCUSSION

In this paper, an experimental investigation is performed on gas entrainment and gas leakage mechanisms of three different flow patterns (i.e., FC, ITC, and CTC) of a ventilated cavity around a conical axisymmetric body. By applying the high-speed digital camera, we can record the instantaneous flow structure of the ventilated cavity body and characteristics of foam shedding at the cavity rear. Based on the observation, the whole cavity can be divided into two distinct regions including the transparent region at the cavity front and the recirculating vortex at the cavity rear. The transparent region occupies increased volume as the cavity grows from FC to ITC and eventually to CTC with increased ventilation rate. More specifically, the gas flow inside the transparent region is further divided into two parts: the internal boundary layer closed to the gas-water interface and reverse flow between the internal boundary layer and the solid cavitator body, according to Wu *et al.* [23]. Based on the experimental observation and past understanding of the cavities, a qualitative analysis of the gas entrainment process in FC, ITC, and CTC is presented. Specifically, in FC, the gas injected into the water flow is immediately entrained by the recirculating vortex, and then the foam shedding is established under the shear of the free stream. In ITC and CTC, the injected gas is immediately entrained into the internal boundary layer in the transparent region at the cavity front and then transported to the reversed region and the recirculating vortex at the cavity rear. The foam shedding is also observed in ITC and CTC. Additionally, it is concluded that the gas leakage for all flow patterns is determined by the physical size and shedding frequency of the foam leaving the cavity at the rear. As the flow pattern varies from FC to CTC with increasing $C_Q$, it is observed that the size of the shedding foam grows larger while the shedding frequency gradually reduces, leading to balanced gas injection and leakage.

Moreover, by combining the visualization results of ventilated cavity geometry and characteristics of gas entrainment and leakage, we quantitatively explain the gas leakage mechanism during the transition from ITC to CTC, in which a slight increase of $C_Q$ leads to significant increase of cavity length (i.e., the ventilated hysteresis). In detail, a quantitative gas leakage model is established by assuming that the foam at the cavity rear is periodically shed in the form of a vortex ring, whose size can be uniquely decided by the cavity geometry. To validate the effectiveness of the model, we firstly compare the measured shedding frequency (represented by St) and cavity geometry (represented by the radius ratio $R_C/R_n$) to relevant past studies. The comparison results show that St is approximately equal to 0.21, consistent with past measurements of flow over a cylinder [54,55]. Additionally, $R_C$ measured under the maximum $C_Q$ is close to the results from Shao *et al.* [32] and Garabedian [49]. Secondly, we develop a constant value $K = 0.36$ to represent the comprehensive impacts of void fraction and turbulent breakup of the vortex ring. Finally, $K$, St, and $R_C/R_n$ are combined in Eq. (2) to calculate the gas leakage $C_Q$. The gas leakage model is validated to be capable of accurately predicting the critical $C_Q$ required for ITC-to-CTC transition for all tested Fr cases.

Furthermore, a physical mechanism with theoretical quantitative analysis is provided to explain the closure mode discrepancy between the CTCs in this paper and the free-standing supercavities obtained by previous studies. Specifically, the presence of the recirculating vortex in CTCs is primarily caused by the large APG in the streamwise direction, which leads to the water flow separation that breaks up the gas-water interface into foams. This large APG is generated under the impact of the stagnation point on the cavitator body, which reduces the water flow velocity to zero and tremendously increases the pressure at the cavity rear. Due to the presence of the cavitator body, the APG of a CTC is estimated to be 6.8 times that of a free-standing supercavity without the inserted cavitator body under same flow conditions.

In this paper, we provided mechanisms of gas entrainment and leakage for a ventilated cavity around a conical axisymmetric body. Moreover, in this paper, we also provided a quantitative model of gas leakage for the flow pattern before the hysteresis (ITC) and a quantitative analysis of the closure mode difference after the hysteresis between our observation (CTC) and previous studies (free-standing supercavity). The gas leakage model is supported by the agreement of Fr and $R_C$ with previous studies [32,49,54,55] and the validation using our own experiment data. Additionally, the quantitative analysis that the large APG causes the water flow separation at the cavity rear is consistent with the observation by Wu *et al.* [23].

## ACKNOWLEDGMENTS

The authors gratefully acknowledge the support by the National Nature Science Foundation of China (No. 12002038, No. U20B2004, and No. 51906017) and Beijing Municipal Natural Science Foundation (No. 3222041).

[1] J. R. Blake and D. C. Gibson, Cavitation bubbles near boundaries, Annu Rev Fluid Mech **19**, 99 (1987).
[2] C. E. Brennen, *Cavitation and Bubble Dynamics* (Oxford University Press, Oxford, 1995).
[3] J.-P. Franc and J.-M. Michel, *Fundamentals of Cavitation* (Kluwer Academic Publishers, Dordrecht, 2005).
[4] R. E. A. Arndt, W. T. Hambleton, E. Kawakami, and E. L. Amromin, Creation and maintenance of cavities under horizontal surfaces in steady and gust flows, J. Fluids Eng. **131**, 111301 (2009).
[5] A. Karn, R. E. A. Arndt, and J. Hong, An experimental investigation into supercavity closure mechanisms, J. Fluid Mech. **789**, 259 (2016).
[6] T. M. Pham, F. Larrarte, and D. H. Fruman, Investigation of unsteady sheet cavitation and cloud cavitation mechanisms, J. Fluids Eng. **121**, 289 (1999).
[7] G. Wang and S. Cao, Ventilation effects on cavitation induced-vibration, J. Hydroelectr. Eng. **2**, 55 (2001).
[8] B. Ji, X.-w. Luo, X.-x. Peng, Y. Zhang, Y.-l. Wu, and H.-y. Xu, Numerical investigation of the ventilated cavitating flow around an under-water vehicle based on a three-component cavitation model, J. Hydrodyn. **22**, 753 (2010).
[9] A. Yu, X. Luo, and B. Ji, Analysis of ventilated cavitation around a cylinder vehicle with nature cavitation using a new simulation method, Sci. Bull. **60**, 1833 (2015).
[10] S. A. Mäkiharju, I.-H. R. Lee, G. P. Filip, K. J. Maki, and S. L. Ceccio, The topology of gas jets injected beneath a surface and subject to liquid cross-flow, J. Fluid Mech. **818**, 141 (2017).
[11] C. Wang, B. Huang, M. Zhang, G. Wang, Q. Wu, and D. Kong, Effects of air injection on the characteristics of unsteady sheet/cloud cavitation shedding in the convergent-divergent channel, Int. J. Multiphase Flow **106**, 1 (2018).
[12] E. L. Amromin and I. Mizine, Partial cavitation as drag reduction technique and problem of active flow control, Mar. Technol. SNAME N. **40**, 181 (2003).
[13] W. C. Sanders, E. S. Winkel, D. R. Dowling, M. Perlin, and S. L. Ceccio, Bubble friction drag reduction in a high-Reynolds-number flat-plate turbulent boundary layer, J. Fluid Mech. **552**, 353 (2006).

[14] Y. Jiang, S.-W. Jeong, B.-K. Ahn, H.-T. Kim, and Y.-R. Jung, Experimental investigation of drag characteristics of ventilated supercavitating vehicles with different body shapes, Phys. Fluids **31**, 052106 (2019).
[15] P. Kumar and R. P. Saini, Study of cavitation in hydro turbines—a review, Renewable Sustainable Energy Rev. **14**, 374 (2010).
[16] C. M. Harwood, Y. L. Young, and S. L. Ceccio, Ventilated cavities on a surface-piercing hydrofoil at moderate Froude numbers: cavity formation, elimination and stability, J. Fluid Mech. **800**, 5 (2016).
[17] S. Shao, A. Karn, B.-K. Ahn, R. E. A. Arndt, and J. Hong, A comparative study of natural and ventilated supercavitation across two closed-wall water tunnel facilities, Exp. Therm Fluid Sci. **88**, 519 (2017).
[18] S. Qin, Y. Wu, D. Wu, and J. Hong, Experimental investigation of ventilated partial cavitation, Int. J. Multiphase Flow **113**, 153 (2019).
[19] H. Reichardt, *The Laws of Cavitation Bubbles at Axially Symmetrical Bodies in a Flow* (Kaiser Wilhelm Institute für Stromungsforschung, Britain 1945).
[20] R. Cox and W. Clayden, Air entrainment at the rear of a steady cavity, in *Proceedings of the Symposium on Cavitation in Hydrodynamics* (HMSO, 1955).
[21] G. V. Logvinovich, *Hydrodynamics of Free-Boundary Flows* (Halsted Press, Russian, 1972).
[22] G. M. Skidmore, *The Pulsation of Ventilated Supercavities*, Master's thesis, The Pennsylvania State University, 2012.
[23] Y. Wu, Y. Liu, S. Shao, and J. Hong, On the internal flow of a ventilated supercavity, J. Fluid Mech. **862**, 1135 (2019).
[24] I. Campbell and D. Hilborne, Air entrainment behind artificially inflated cavities, in *Proceedings of the Second Symposium on Naval Hydrodynamics* (Washington, DC, 1958), pp. 467.
[25] J. Spurk, On the gas loss from ventilated supercavities, Acta Mech. **155**, 125 (2002).
[26] E. Kawakami and R. E. A. Arndt, Investigation of the behavior of ventilated supercavities, J. Fluids Eng. **133**, 091305 (2011).
[27] A. Karn, R. E. A. Arndt, and J. Hong, Dependence of supercavity closure upon flow unsteadiness, Exp. Therm Fluid Sci. **68**, 493 (2015).
[28] Y. Kapankin and A. Gusev, Experimental research of joint influence of fluid and lift power of cavitator on character of flow in cavity rear part and gas departure from it, *Proc. CAHI* (Moscow, Russia, 1984), p. 19.
[29] E. Silberman and C. S. Song, Instability of ventilated cavities, J. Ship Res. **5**, 13 (1961).
[30] Y. Lv, M. Zhang, T. Liu, J. Chen, B. Huang, and L. Hao, Physical and numerical study on the transition of gas leakage regime of ventilated cavitating flow, Ocean Eng. **239**, 109861 (2021).
[31] S.-J. Lee, E. Kawakami, A. Karn, and R. E. A. Arndt, A comparative study of behaviors of ventilated supercavities between experimental models with different mounting configurations, Fluid Dyn. Res. **48**, 045506 (2016).
[32] S. Shao, A. Balakrishna, K. Yoon, J. Li, Y. Liu, and J. Hong, Effect of mounting strut and cavitator shape on the ventilation demand for ventilated supercavitation, Exp. Therm Fluid Sci. **118**, 110173 (2020).
[33] T. Liu, B. Huang, G. Wang, M. Zhang, and D. Gao, Experimental investigation of the flow pattern for ventilated partial cavitating flows with effect of Froude number and gas entrainment, Ocean Eng. **129**, 343 (2017).
[34] T. Liu, B. Huang, G. Wang, and M. Zhang, Experimental investigation of ventilated partial cavitating flows with special emphasis on flow pattern regime and unsteady shedding behavior around an axisymmetric body at different angles of attack, Ocean Eng. **147**, 289 (2018).
[35] T. Sun, X. Zhang, C. Xu, G. Zhang, C. Wang, and Z. Zong, Experimental investigation on the cavity evolution and dynamics with special emphasis on the development stage of ventilated partial cavitating flow, Ocean Eng. **187**, 106140 (2019).
[36] T. Sun, X. Zhang, C. Xu, G. Zhang, S. Jiang, and Z. Zong, Numerical modeling and simulation of the shedding mechanism and vortex structures at the development stage of ventilated partial cavitating flows, Eur. J. Mech. B. Fluids **76**, 223 (2019).
[37] L. Wang, B. Huang, S. Qin, L. Cao, H. Fang, D. Wu, and C. Li, Experimental investigation on ventilated cavity flow of a model ship, Ocean Eng. **214**, 107546 (2020).

[38] See Supplemental Material at http://link.aps.org/supplemental/10.1103/PhysRevFluids.7.123901 for experimental movies of three distinguishable flow patterns (Video 1) and each flow pattern: FC (Video 2), CFC (Video 3), and CTC (Video 4).
[39] S. Corrsin and A. L. Kistler, *Free-Stream Boundaries of Turbulent Flows* (National Advisory Committee for Aeronautics, Washington, DC, 1955).
[40] C. Meneveau and K. R. Sreenivasan, Interface dimension in intermittent turbulence, Phys. Rev. A **41**, 2246 (1990).
[41] J. E. Cooper, in *Encyclopedia of Vibration*, edited by S. Braun (Elsevier, Oxford, 2001), pp. 87.
[42] L. Skrbek and W. F. Vinen, in *Progress in Low Temperature Physics*, edited by M. Tsubota, and W. P. Halperin, (Elsevier, Amsterdam, 2009), pp. 195–246.
[43] Z. Wang, B. Huang, M. Zhang, G. Wang, and X. a. Zhao, Experimental and numerical investigation of ventilated cavitating flow structures with special emphasis on vortex shedding dynamics, Int. J. Multiphase Flow **98**, 79 (2018).
[44] P. Ausoni, M. Farhat, Y. Ait Bouziad, J.-L. Kueny, and F. Avellan, Kármán vortex shedding in the wake of a 2D hydrofoil: Measurement and numerical simulation, in *IAHR Int. Meeting of WG on Cavitation and Dynamic Problems in Hydraulic Machinery and Systems* (EPFL, Barcelona, 2006).
[45] R. Franke, W. Rodi, and B. Schönung, Numerical calculation of laminar vortex-shedding flow past cylinders, J. Wind Eng. Ind. Aerodyn. **35**, 237 (1990).
[46] F. Stella, N. Mazellier, and A. Kourta, Scaling of separated shear layers: an investigation of mass entrainment, J. Fluid Mech. **826**, 851 (2017).
[47] Y. N. Savchenko, Supercavitation—problems and perspectives, in *CAV 2001: Fourth International Symposium on Cavitation* (California Institute of Technology, Pasadena, 2001).
[48] M. Dular and R. Bachert, The issue of Strouhal number definition in cavitating flow, J. Mech. Eng. **55**, 9 (2009).
[49] P. Garabedian, Calculation of axially symmetric cavities and jets, Pac. J. Math. **6**, 611 (1956).
[50] A. May, *Water Entry and the Cavity-Running Behavior of Missiles* (NAVSEA Hydroballistics Advisory Committee, Silver Spring, 1975).
[51] S.-J. Lee, B.-G. Paik, K.-Y. Kim, Y.-R. Jung, M.-J. Kim, and R. E. A. Arndt, On axial deformation of ventilated supercavities in closed-wall tunnel experiments, Exp. Therm Fluid Sci. **96**, 321 (2018).
[52] W. Zou, K. Yu, R. E. A. Arndt, and E. Kawakami, On minimum cavitation number of the ventilated supercavity in water tunnel, Sci. China Phys. Mech. Astron. **56**, 1945 (2013).
[53] Y. Jiang, S. Shao, and J. Hong, Experimental investigation of ventilated supercavitation with gas jet cavitator, Phys. Fluids **30**, 012103 (2018).
[54] A. Roshko, *On the Development of Turbulent Wakes From Vortex Streets* (National Advisory Committee for Aeronautics, Washington, DC, 1953).
[55] E. L. Houghton and P. W. Carpenter, *Aerodynamics for Engineering Students* (Butterworth-Heinemann, Burlington, 2003).
[56] X. Liu and J. Katz, Vortex-corner interactions in a cavity shear layer elucidated by time-resolved measurements of the pressure field, J. Fluid Mech. **728**, 417 (2013).